Polymer Testing 128 (2023) 108194

Contents lists available at ScienceDirect

Polymer Testing

journal homepage: www.elsevier.com/locate/polytest

Research paper

Fatigue mechanisms of a closed cell elastomeric foam: A mechanical and microstructural study using *ex situ* X-ray microtomography

C. Aimar [a,b], L. Orgéas [a,*], S. Rolland du Roscoat [a], L. Bailly [a], D. Ferré Sentis [b]

[a] Univ. Grenoble Alpes, CNRS, Grenoble INP, 3SR Lab, Grenoble, 38000, France
[b] Decathlon SA - Footwear International Division, Wattrelos, 59150, France

ARTICLE INFO

Keywords:
Closed cell elastomeric foams
Fatigue
Compression test
Damage mechanisms
X-ray microtomography
Memory effects

ABSTRACT

The degradation of mechanical properties of closed-cell elastomeric foams in fatigue and its link with the cellular structure is still poorly understood. To clarify this, we performed interrupted and continuous cyclic compression tests on EVA closed-cell foams used in running shoes. The 3D cellular structures of tested samples was analyzed before, during and after fatigue tests using X-ray microtomography and digital volume correlation. Interrupting the cycling allows the observation of the cell flattening along the compression axis with both plastic bending and an increase of tears/holes of cell walls. These two fatigue-induced defects are suspected to play a strong contribution on the fatigue properties of the foam at the sample scale and may explain the partial recovery of the initial mechanical property of foams while restarting cycling.

1. Introduction

Owing to their excellent specific mechanical properties, cellular elastomeric materials are often used as structural absorbing systems in many fields such as automotive industry, packaging and sport gear [1–3]. If the fatigue of bulk elastomeric materials has been widely studied in elongation, compression and shear deformation modes [4–9], the fatigue of elastomeric foams was, on the contrary, less analyzed [10–12]. Specifically, studies devoted to the fatigue of closed cell elastomeric foams are scarce. The field of sport running shoes, the midsoles of which are made of closed cell elastomeric foams, is the rare case where few studies have documented the fatigue in compression of such foams, here designed to absorb and to restitute a maximum of energy with optimal specific mechanical strength and stiffness [13]. Analyzing their fatigue (micro)mechanisms represents a challenging task as these systems are sequentially deformed at cyclic finite strains and exhibit complex compressible elastoviscoplastic behavior [14].

Over the past 40 years, the midsole foams of sport running shoes are mainly made of ethylene-vinyl-acetate (EVA) [15,16], due to their low-cost and their fast and versatile manufacturing process. Thus, the fatigue of EVA foams are by far the most studied closed cell foams in the literature [17–22]. Among these works, only a few studies investigated interrupted compression fatigue tests in laboratory. Verdejo et al. set up a daily two hours interrupted impact fatigue procedure during 5 days in a row [23]. They observed a partial recovery of the peak force level during resting time, coupled with a global softening of the samples over the week. Allen et al. compared a continuous and an interrupted procedure [15]. The authors found that samples partially recovered their energy absorption capabilities during a daily rest period and concluded that foams lose faster this property in a continuous fatigue procedure equivalent to 60 km. In their perspective, Allen et al. suggested to observe the microstructure of foams after fatigue test and recovery. Unfortunately, the proposed fatigue procedure was short compared to the shoe lifetime. In addition, fatigue-induced microstructures of deformed foams were not observed. More recently, longer continuous fatigue tests of closed cell EVA foams have been reported to mimic a long distance running up to 160 km [19,24,25]. The deformed foams exhibited a progressive softening of their stress–strain responses which was faster during the first 5000 cycles than afterwards. The cyclic behavior of EVA foams were also studied on commercial shoes during and after real training sessions [13,16,26]. Verdejo et al. were among the first authors to study the link between mechanical and structural properties of such elastomeric closed cell foams in fatigue. Using scanning electron microscopy (SEM), they compared the structures of different EVA foam samples collected before and after 500 km and 700 km of running sessions. The cell walls of foams exhibited buckling and holes of about 10–20 μm [16], revealing some structural damages. However, the sample preparation used for SEM (*e.g.*, prepared after dipping the sample in liquid nitrogen) might have affected the observed

* Corresponding author.
E-mail address: laurent.orgeas@3sr-grenoble.fr (L. Orgéas).

https://doi.org/10.1016/j.polymertesting.2023.108194
Received 12 June 2023; Received in revised form 23 August 2023; Accepted 7 September 2023
Available online 12 September 2023

foams and thus altered the drawn conclusions [27]. In addition, variations in the foam microstructures (local densities, pore and cell sizes, shape and anisotropy) due to manufacturing processes prevent to study deformation micro-mechanisms on *post-mortem* samples in the absence of a proper comparison with their initial microstructure. Hence, to date, the links between the mechanical changes of EVA foams and their 3D microstructural evolution have never been analyzed, during continuous or interrupted fatigue procedures with a coupled mechanical and microstructural approach.

Over the past two decades, X-ray tomography combined with 3D image analysis has been widely used to study morphologies of metal, ceramic and polymer based foams [27–31]. More recently, this 3D imaging technique became a promising tool to observe fatigue-induced fracture initiation and propagation in brittle foams [32] although it has never been used to study the fatigue of elastomeric foams. Beyond the preservation of the bulk structures of imaged samples, the technique offers the opportunity to quantify their 3D microstructural descriptors without extrapolation from 2D images such as with SEM or optical observations [33]. Thus, 3D *in-situ* observations using X-ray microtomography were carried out during monotonic compression tests (and sometimes combined with finite element analysis or digital volume correlation) to quantify the deformation mechanism at the cell wall scale in elastomeric foams [34,35]. However, microstructural descriptors commonly used to describe the cellular morphology of foams (such as the porosity, the thickness of walls, the size of cells as well as the degree of anisotropy [36]) were not intensively utilized to quantify and discuss the observed deformation micromechanisms. In addition, to the best of our knowledge, no study has been reported in the literature to investigate fatigue-induced structural evolutions in the considered cellular systems, whereas X-ray tomography was proved to be a proper relevant techniques to investigate, *e.g.* via 3D *ex situ* observations, fatigue or other structural evolutions in other cellular materials [37–40].

Thus, the objective of the present work is to investigate the links between the structural evolutions and the mechanical fatigue of closed cell elastomeric foams during continuous or interrupted finite strain cyclic compression. To meet this objective, we developed a methodology to monitor, during cyclic compression, the cellular structures of EVA foams with 3D and 2D *ex situ* observations using X-ray microtomography and SEM.

2. Materials and methods

2.1. Materials

We studied the fatigue of an EVA foam formulation which is used for the midsoles of running shoes [41]. The foam was supplied by Yuede (Binh Thanh District, Vietnam) under the form of slabs (dimensions: 245 × 147 × 10 mm^3) and produced by compression molding. Samples were preserved at 55%RH and 23°C from reception to the end of experiments. The solid phase was made of 81 wt% of an EVA blend average vinyl-acetate content: 22 wt% and average polyethylene content: 78 wt%, 10 wt% of diluting micron-sized mineral fillers ($CaCO_3$) and 9 wt% of other chemicals and additives to ease the process. The 2 mm upper and lower skins of the foam slab was removed using a slitter machine (Fortuna AB 320G) and the density of the core sheet was measured using a caliper (Mitutoyo, precision: 0.1 mm) and a microbalance (Mettler Toledo, precision: 0.1 mg). Small cylindrical samples (initial height $h_0 \approx 2$ mm and diameter $d_0 \approx 2$ mm) were dye cut in the core sheet using a punch and used for structural and mechanical characterizations (see below).

2.2. Fatigue tests

Finite strain cyclic compression - These tests were performed using an electromechanical tension–compression testing machine (Instron 05994) equipped with a ± 10 N maximal load capacity sensor (Fig. 1a). During the tests, the force f_z was recorded to calculate the nominal compression stress $\sigma_{zz} = -4f_z/(\pi d_0^2)$ and the compression Hencky strain $\varepsilon_{zz} = -\ln(h/h_0)$ was derived from the displacement δ of the cross-head (with $h = h_0 - \delta$ and where compression stress and strains have been arbitrarily set as positive values). During cyclic compression, samples were repetitively subjected to identical load–unload sequences up to a maximal strain $\varepsilon_{zz}^{max} = 1.6$ (which corresponds to the maximal compression strain undergone during a stride [42]) at a strain rate of $|\dot{\varepsilon}_{zz}| = 4\ s^{-1}$ (which approximately corresponds to the mean strain rate observed during the cyclic period of a stride of about 0.8 – 0.9 s [42]). Four properties were monitored during cycling: the maximal stress σ_{zz}^{max} at the end of each loading, the residual strain ε_{zz}^{res} at the end of each unloading, the maximum absorbed energy per unit of volume W_{abs}^{max} and the damping loss factor η [43].

Recovery - Regardless of the considered cycling procedure, *i.e.*, interrupted or continuous cycling (see below), we measured the strain recovery of samples just after each cycling sequence, to assess viscoelastic effects at rest. For that, we used a LED screen placed behind the sample and a Nikon D3000 camera with a 180 mm lens as shown in Fig. 1b. Photographs of the samples were recorded every 90 s during 6 h. Thresholding the acquired imaged was easily achieved using the freeware Fiji [44] so that we could estimate the time-evolution of the sample height h and the recovery strain ε_{zz} from its residual strain ε_{zz}^{res} up to its irreversible plastic strain ε_{zz}^{p}.

2.3. Structural characterization

2D observations - The structure of the samples were also characterized at microscale using a SEM (Zeiss, Ultra55). Samples were cut across the plane parallel to the loading direction using a razor blade to avoid possible fracture induced by the sample cryogenics. A thin carbon film (10 nm in thickness) was laid by evaporation on the cross section of the samples.

3D observations - The structures of the samples were characterized at macro and microscale by using a laboratory X-ray microtomograph (RX-Solution, SIMAP laboratory), the reconstruction software X-Act (based on filtered backprojections) as well as two different conical X-ray sources allowing to obtain two voxel sizes: 100^3 μm^3 and 1 μm^3 [41]. For that purpose, the main acquisition parameters were respectively set to the following values: acceleration voltage of 140 kV and 40 kV, number of projections: 1400 and 2500, scan time: 20 min and 3 h. We used a large voxel size to characterize spatial heterogeneities in the produced slab and to choose proper locations to extract fatigue samples, whereas the small voxel size was used to finely characterize the initial and fatigue-induced microstructures of tested samples. For small voxel size, we extracted regions of interest (ROIs) of 1000^3 μm^3 in the center of the 3D images in order to avoid edge effects from image acquisition-reconstruction. Typical corresponding orthogonal slices in gray levels obtained from an initial EVA foam samples are shown in Fig. 2a and b. From these ROIs, the following image analysis procedures were carried out.

Image registration and local image correlation on 3D images - For spatial registration of the 3D images acquired before and during cycling, we used successively the *ereg* and *reg* functions of the freeware *SPAM* [45], based on Digital Volume Correlation (DVC) procedures. Thus, *SPAM* allowed us to extract the transformation matrix between the initial 3D image of a tested sample and the one obtained after cycling, so that the global transformation gradient **F** of the sample could be estimated,

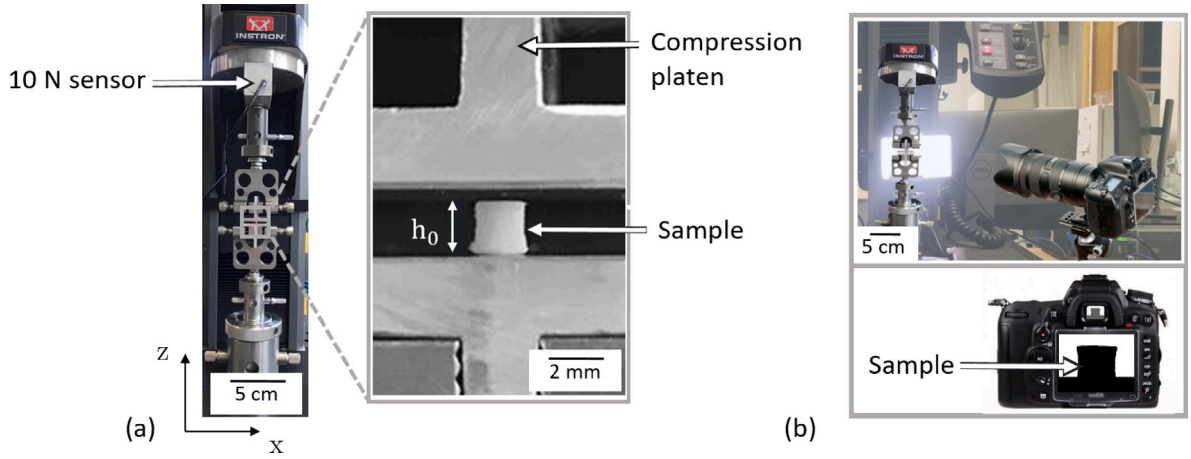

Fig. 1. (a) Compression device with a zoom on a sample mounted between the compression platens. (b) View of the set-up used to estimate the recovery strain after cycling (led screen placed behind the sample + camera).

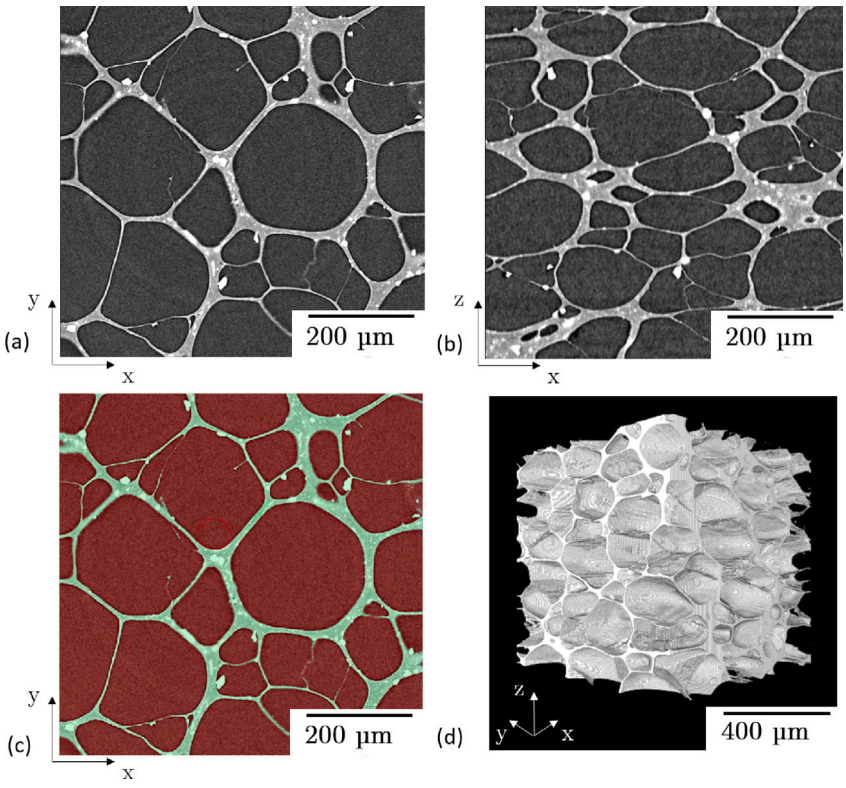

Fig. 2. 2D slices orthogonal (a) or parallel (b) to the compression axis z of an underformed foam sample. Slice (a) (in c) and 3D view of the ROI (d) after proper segmentation using the Weka segmentation plugin.

from which the Hencky strain tensor was computed $\varepsilon^{\mathbf{p}} = -\ln(\sqrt{\mathbf{F}^T \cdot \mathbf{F}})$ in order to estimate its principal components as well as the sample volumetric strain $\varepsilon^p_{vol} = \varepsilon^p_{xx} + \varepsilon^p_{yy} + \varepsilon^p_{zz}$. These strains components and invariant correspond to plastic strain measures after 24 h (see Results).

Image segmentation on 3D images - The Weka Segmentation plugin [46] of Fiji was used for the image segmentation. It is based on a fast random forest algorithm to segment very thin cellular walls < 2 µm (Fig. 2c). During the first part of the procedure, we defined the number of classes or segments and trained the classifier by giving examples of the zones associated to each class. Two features of the plugin were used (the mean and the variance of grey level values of neighbor voxels) to refine the identification of the segments. The trained classifier was then loaded and used for the next microstructures. The resulting 3D volume of a region of interest was plotted using the plugin 3D viewer [47] (Fig. 2d).

Quantification of microstructural descriptors on 3D images - Five descriptors were assessed on each segmented volume to quantify the structural evolution of samples during fatigue tests: (i) the porosity ϕ which was obtained by dividing the number of pore voxels (Fig. 2d) by the total number of voxels in the ROI, (ii) the apparent volumetric number of pores $\mathcal{N}_p$, *i.e.*, the volumetric number of the sets of connected unit cells at the considered spatial resolution, (iii) the volumetric number of cell $\mathcal{N}_c$, (iv) the average intrinsic volumetric strain of cells ε^{cell}_{vol} and (v) the average cell degree of anisotropy DA. For the second descriptor, $\mathcal{N}_p$, we used the plugin *Analysis 3D* of Fiji [48] to find (based on a marching cube algorithm) and label the pores in the 3D images, except those on the boundaries of the ROIs. For the three last descriptors, each cell

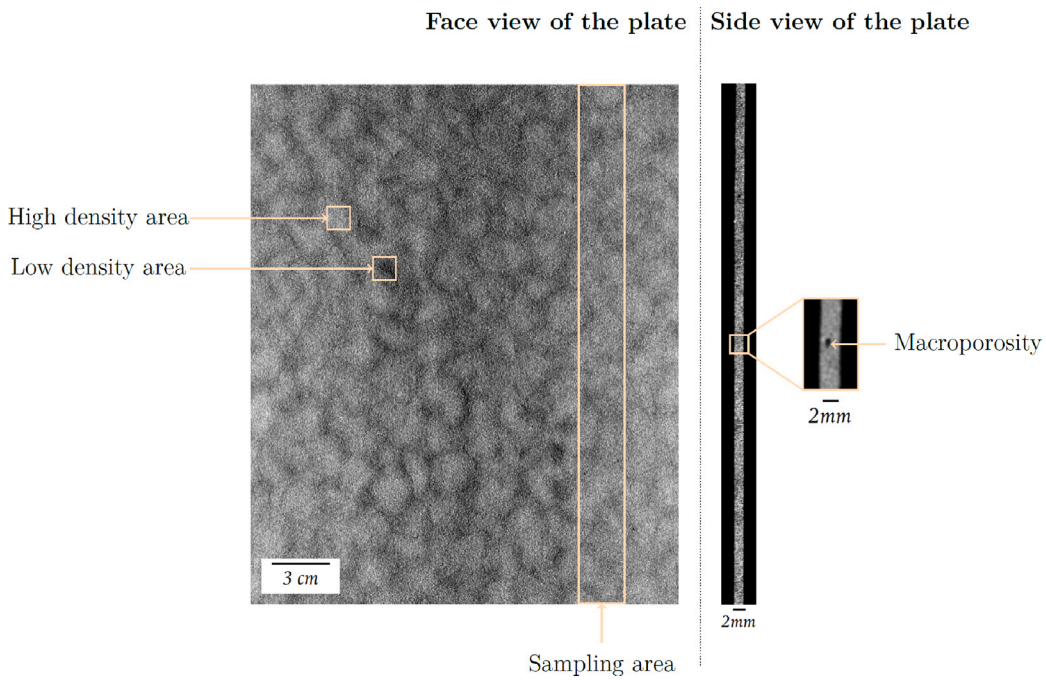

Fig. 3. Orthogonal slices showing the in-plane (left) and the out-of-plane (right) macroscale heterogeneities in the core of the tested slab produced by compression molding.

contained in each studied ROI were first isolated using a 3D watershed algorithm and then re-labeled using the plugin *Analysis 3D*. The plugin provided the volume of each labeled cell v^{cell}, from which the cell volume strain $e_{vol}^{cell} = -\ln(v^{cell}/v_0^{cell})$ was estimated. The plugin also gave the major I_{max} and minor I_{min} elements of inertia of each labeled cell, from which the cell degree of anisotropy $da = 1 - I_{min}/I_{max}$ was estimated. Its values range between 0 and 1 (0 for a perfectly isotropic cell). Therefrom, ϵ_{vol}^{cell} (resp. the DA) was then calculated as the average value of the e_{vol}^{cell} (resp. da) obtained from 10 different cells.

2.4. Testing procedures

We used two testing procedures to characterize the mechanical behavior together with the microstructures of the EVA foam samples during cyclic compression, namely an *interrupted* one and a *continuous* one. Both of them consisted in getting an initial 3D and 2D image of the microstructure of each tested sample. Then, the *interrupted* procedure consisted in 3 consecutive sequences made of (i) cyclic compression, followed by (ii) a resting time of 24 h (the minimum rest period of a runner and his shoes) during which (a) the recovery of the tested sample was assessed (immediately after step (i)), (b) a 3D image of the sample was recorded (4 h before the end of the resting time, *i.e.,* when recovery was ended) and (c) 2D images of a sample after each fatigue sequence was also recorded. For the first sequence, 1000 compression cycles were performed in step (i). This corresponds to 15 min of running, *i.e.*, the average warm-up of a runner. For the second sequence, 4000 compression cycles were performed in step (i), which corresponds to a training session of 1 h. Step (i) in the third and last sequence was made of 195 000 compression cycles, which is equivalent of a running time of 44 h, *i.e.*, the maximum time to run the international Mont-Blanc ultra-trail race. The *continuous* procedure was similar to one of the aforementioned sequences with, however, 200 000 compression cycles performed during step (i), *i.e.*, the total number of compression cycles carried out in the *interrupted* procedure.

3. Results and discussion

3.1. Structural characterization in the initial state

At the millimeter scale – The orthogonal slices shown in Fig. 3 illustrate the millimeter scale variations of the foam density inside the tested slab (grey levels are proportional to the foam density, see the scale bar). As evident from this figure, important density gradients of $\pm$ 0.03 g cm^{-3} around the mean slab density (which is close to 0.17 g cm^{-3}) are observed with the presence of numerous centimeter-large flocks, and with some rare macropores: these defects were induced by the compression molding process. Thus, in order to minimize the variability of our structural and mechanical results shown hereafter, we selected the sampling area shown in the figure to extract the cylindrical samples. In this zone, the grey levels belonged to the mean-grey level zones (*i.e.*, mean-density zones): only the extracted cylindrical samples with a density equal to 0.17 $\pm$ 0.01 g cm^{-3} were kept for the study.

At the micron scale – Figs. 2 and 4a and b show the typical initial microstructures of the tested samples. It is worth noting that below the voxel size, details about the microstructures cannot be captured, *e.g.*, small cell walls, hole in cell walls or mineral fillers. Bearing in mind this remark, these figures prove that the studied foams exhibit convex cells, with a porosity close to $\phi = 0.817 \pm 0.008$ (Fig. 4a) and $\phi = 0.818 \pm 0.005$ (Fig. 4b) for the samples used for interrupted or continuous fatigue procedures, respectively. The other assessed initial microstructures descriptors are also practically identical : for instance, the average degree of anisotropy DA is close to 0.42 ± 0.04 whatever the considered sample and related cycling procedure. Thus, a comparison of their mechanical and structural evolution under the two fatigue procedures is consistent. More precisely, the initial mean cell volume v_0^{cell} is close to 3.5 10^6 µm^3, which yields to a characteristic pore size of $\approx$ 138 µm. In addition, the cells clearly display rounded cells in the (x, y) plane (Figs. 2a and 4) and elliptical shape perpendicular direction (Fig. 2b). This transverse isotropy is directly connected to the compression molding process. In addition, most of the cell walls are rather flat, even if few of them exhibit wavy/buckled shapes. Also, one can notice from these figures that poorly dispersed mineral fillers are

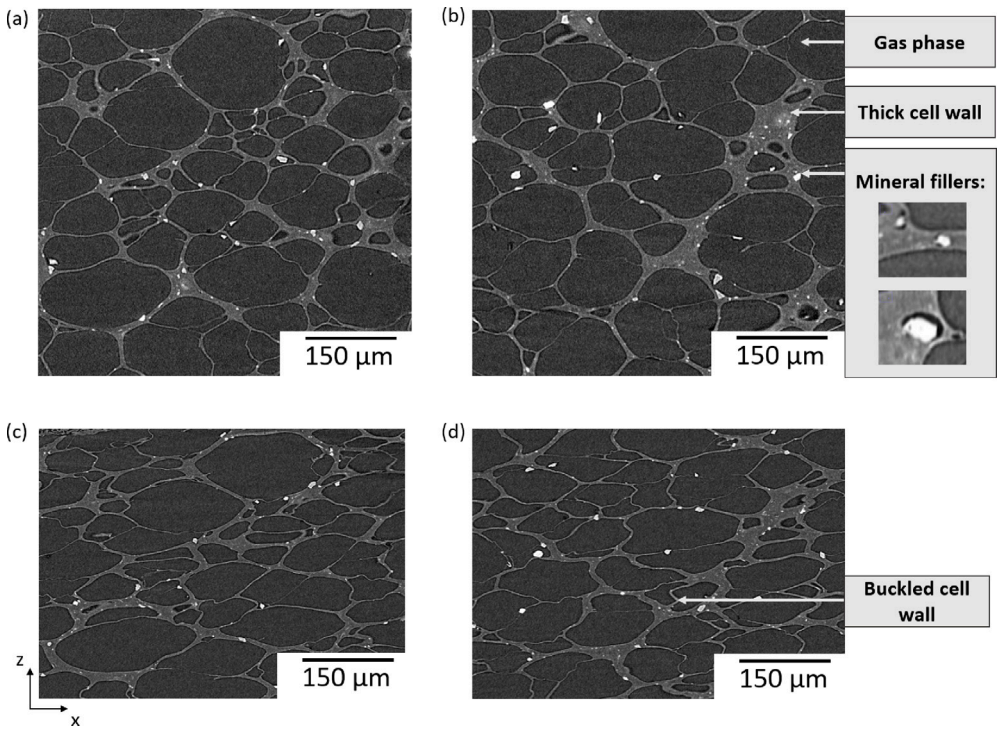

Fig. 4. Slices of the initial microstructures of samples used for the (a) interrupted and the (b) continuous cycling procedures. Same microstructures (after image registration) corresponding to the (c) interrupted and to the (d) continuous procedures at the end of cycling, *i.e.*, at $N = 200000$.

observed in the microstructures and are also seen in Fig. 12, either in cell walls or onto their surfaces. Their volume fraction is 0.6% and their size lies between 2 and 25 µm. It is interesting to note, as exemplified from the zoom shown in Fig. 4, that the interfaces between the mineral charges and the EVA are often imperfect, with initial decohesioned zones. Lastly, the estimation of the numbers of pores and cells in the initial tested samples proves that $\mathcal{N}_p \approx 0.95\mathcal{N}_c$ so that the studied foam mainly exhibit closed cells with, however, $\approx 5\%$ of initially connected cells.

3.2. Fatigue tests

Cyclic loadings - Fig. 5a to c present typical stress–strain curves recorded during cycling in steps 1, 2 and 3 of the interrupted procedure, respectively. Fig. 5d to f show similar graphs but at $N = 1, 1001, 5001$, $N = 1000, 2000$, and $N = 5000, 6000$, respectively. We have also reported in Fig. 6 the evolution of the maximal stress σ_{zz}^{max}, the residual strain ε_{zz}^{res} as well as the absorbed W_{abs}^{max} and the damping loss factor η as functions of the number of cycles N. These results bring up the following comments:

- The shape of stress–strain curves during the first load–unload (see Fig. 5a at $N = 1$) is typical to EVA closed-cell foams or other elastomer closed-cell foams, presenting three recognized densification regimes during load with a residual strain of 0.15 and a rather high damping loss factor close to 0.13. The high elastic character of the observed stress–strain curves is ascribed both to the elasticity of the cell wall elastomer and to the (reversible) compressibility of the gas entrapped in the cells. The hysteresis also observed in stress–strain curves can be related to the viscoelasticity of the elastomer and to possible time-dependent transport of gas in/out of the cells (due to holes or to diffusion mechanisms, the latter being negligible upon cycling [23]), to plastic events in the cell walls such as, for example, friction mechanisms at the interfaces between the mineral fillers and the EVA.
- The decrease in the stress levels and hysteresis area together with the increase of the residual strain between the 1^{st} and the 1000^{th} cycles of each step is similar for the three steps (see Fig. 5a, b and c respectively at $N = 1$ and 1000, $N = 1001$ and 2000, $N = 5001$ and 6000). Such a softening of the material is typical of elastomeric foams used for midsoles [23,41] and could be ascribed to viscoelastic effects or to plastic ones (see "recovery subsection"). These effects are also clearly evidenced in Fig. 6. Indeed, upon cycling, the maximal stress σ_{zz}^{max} undergo a progressive loss of $\approx 60\%$ at the end of the cycling procedures, the absorbed energy W_{abs}^{max} and the damping loss factor coefficient η also display respective drops of $\approx 70\%$ and $\approx 30\%$, whereas the residual strain exhibit a shift up to 0.8. These results are in-line with those reported in the literature for similar foams [23,41]. In addition, Fig. 6 proves that the damping loss factor exhibit an intermediate increase around $N = 1000$ cycles. This could be related to the occurrence of microstructure changes induced by the damage of cell walls, such as the possible holes that would enhance (viscous) gaz flow through neighboring cell walls, and the increase of the decohesion of the interfaces between the mineral fillers and the EVA. Also, it is worth mentioning that at the end of cycling, each of these mechanical descriptors reach respectively the same values, independently of the considered cycling procedure, *i.e.*, interrupted or continuous.
- Stress–strain curves observed at the end of step 1, *i.e.*., at $N = 1000$, exhibit lower stress levels, absorbed energy, loss coefficient and higher residual strain than their respective values recorded after a 24 h of resting time, *i.e.*, at $N = 1001$. In turn, values reported at $N = 1001$ are closer from those reported at $N = 1$. Identical observations can be stated by comparing the same features at $N = 5000$ and 5001. In addition, in Fig. 5d, the maximal stresses σ_{zz}^{max} of the 1st cycle of step 2 and 3 (resp. $N = 1001$ and $N = 5001$) reach only 90% of 1st of step 1 ($N = 1$). Meanwhile, a plastic strain is observed at the beginning of the loading, *i.e.*, 24 h after a resting period. These results show that foams partially recover their initial mechanical properties and shape between

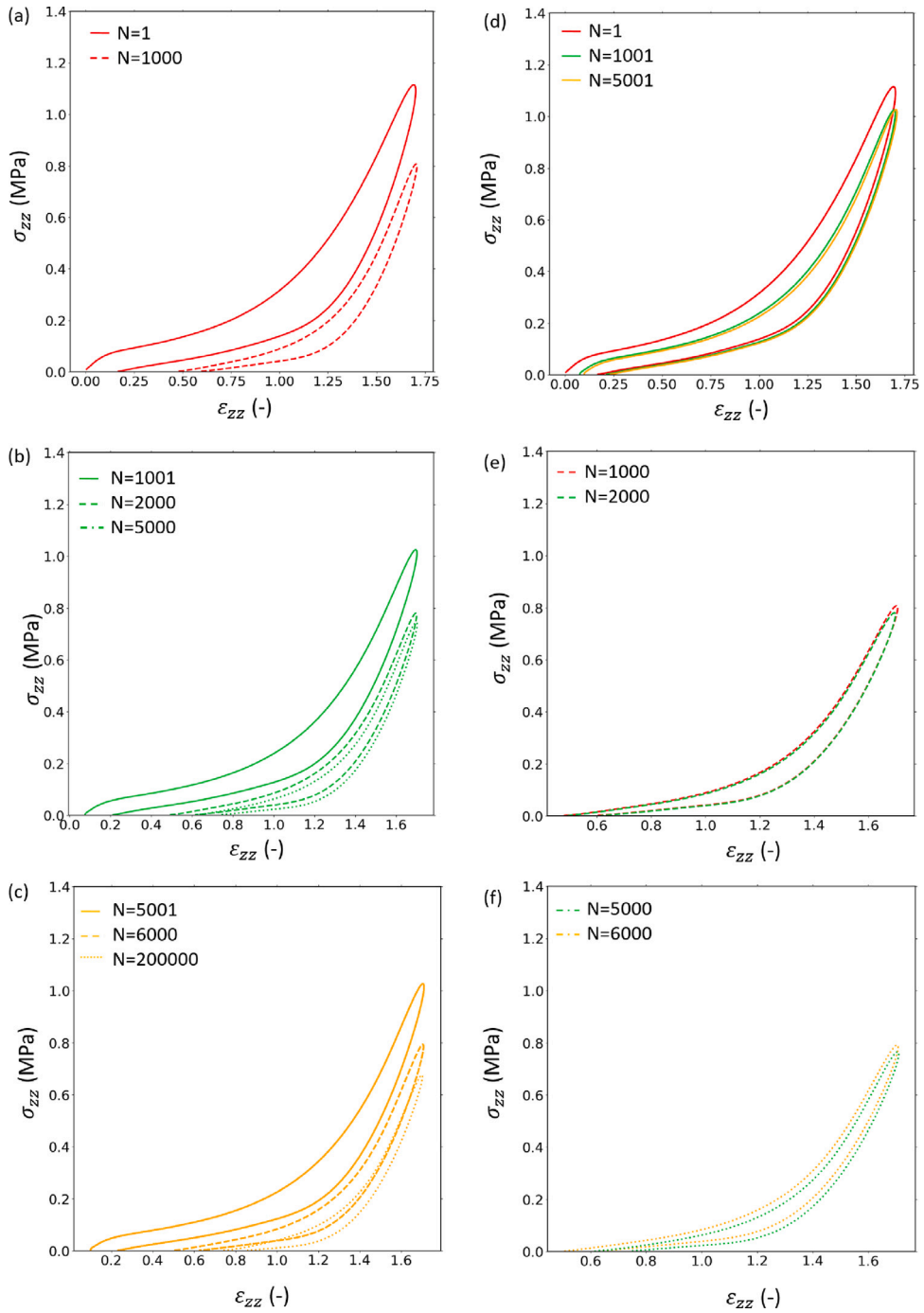

Fig. 5. Stress–strain curves of EVA foam during (a) step 1, (b) step 2 and (c) step 3 of the interrupted procedure. Comparison of (d) the 1st cycles of step 1, 2 and 3, (e) the last cycle of step 1 with the 1000th cycle of step 2, (f) the last cycle of step 2 with the 1000th cycle of step 3.

two consecutive steps of the interrupted procedure, *i.e.*, after a significant resting time. This is in-line with what was observed previously during other interrupted fatigue tests carried out on elastomeric foams [23].

- Stress–strain curves shown in Fig. 5e practically exhibit the same behavior at $N = 1000$ (step 1), $N = 2000$ (step 2). Similarly, stress–strain curves shown in Fig. 5f are identical when $N = 5000$ (step 2) and $N = 6000$ (step 3), as if the partial memory effect induced during the resting time of the end of the preceding sequence vanished. The erasable memory of transient fatigue sequence with in the same time the recovery memory of what happened continuously since the initial state is further illustrated in Fig. 6. Indeed, as evident from the whole graphs of the figure, it is interesting to notice that either the maximal stress, or the residual strain, or the absorbed energy, or the loss coefficient recorded during the interrupted cycling procedure follow those recorded during the continuous one, after a transient period of ≈ 1000 cycles, as if the continuous trends yielded to master curves of the interrupted ones, once a transient regime is achieved. It must be pointed out that similar memory effects were observed by Allen et al. regarding the maximum absorbed energy on a 3 consecutive impact fatigue tests of 10 000 cycles separated by a 22 h of a rest period [15]. The authors found that after the first resting time, the maximum absorbed energy value was comparable (within measurement error and sample consistency) to those

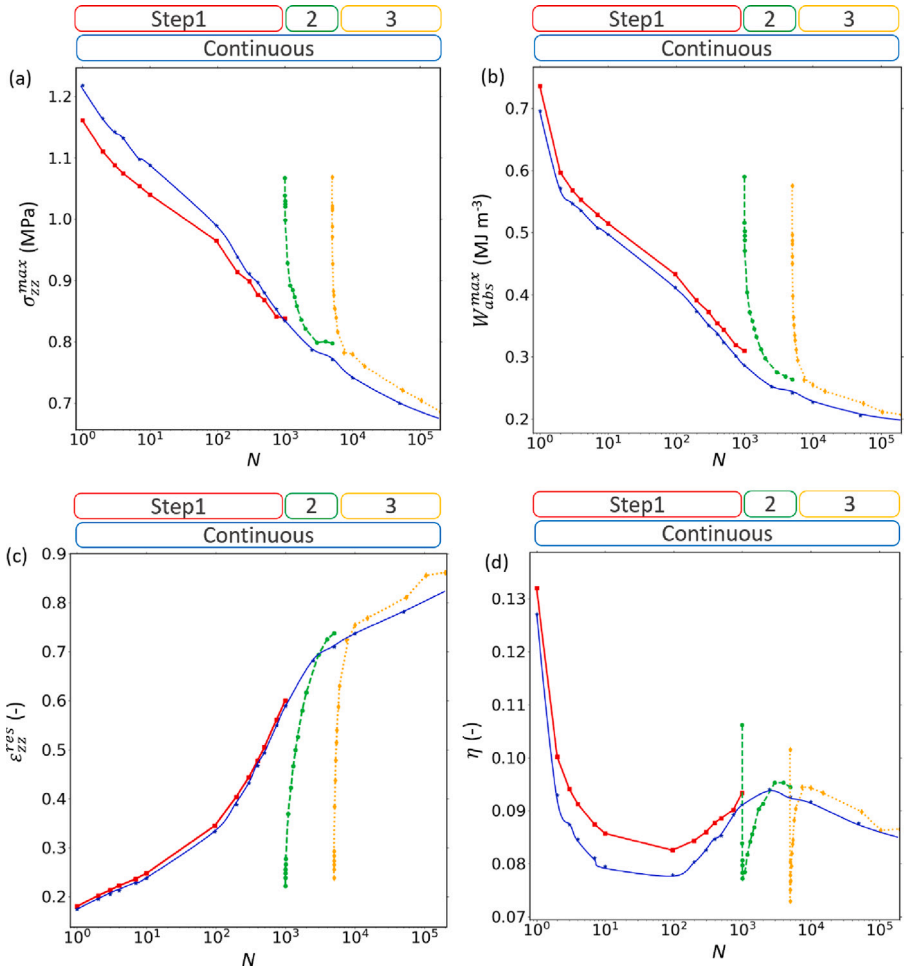

Fig. 6. Evolutions with the number of cycles N of the maximal stress σ^{max} (a), the residual strain ε_{zz}^{res}, the absorbed energy W_{abs}^{max} (c), and the damping loss factor η (d) during the interrupted and the continuous procedure.

reported at the start of the first ageing period and decrease in a similar manner.

Recovery - Fig. 7 shows the time-evolution of the axial residual strain ε_{zz}^{res} (assessed using photo-contrast) right after the end of each cycling sequence compression of the interrupted or the continuous cycling procedures. The inset is a zoom of the early stages of the recovery strain as a function of $\sqrt{t}$. In addition, we have reported in Fig. 8 the evolution of the major strain components ε_{xx}^{p}, ε_{yy}^{p} and ε_{zz}^{p} as well as the volumetric strain ε_{vol}^{p}, as determined from X-ray microtomography and digital image correlation. Several comments can be stated from these figures:

- Whatever the considered sequence and cycling procedure, the graphs of Fig. 7 show that the residual strain after cycling systematically diminish (i) rapidly in the early stages of recovery (ii) towards a steady state irreversible, namely plastic value ε_{zz}^{P}. This time-dependent spring-back regime is probably related to viscoelastic effects often observed in solid polymers/elastomers. In the case of the studied EVA foams, such a recovery could also be (i) assisted by the pressure of the gas entrapped in the cells and (ii) restrained by (a) the viscous flow of the gas through connected cells and, if the cell connectivity is sufficiently high to generate a percolating network, (b) a progressive filling back of the amount of the gas that was initially entrapped in the cells and that could have been expelled out of the sample during mechanical cycling at finite strains (see next subsection).
- It is also interesting to notice that the transient regime exhibit (at least, and phenomenologically) two diffusive-like regimes, as emphasized by the tangent dotted lines plotted in the inset graph of Fig. 7. The higher the initial residual strain, the higher the related characteristic times. For example, the inset of the figure show that the characteristic time of the first regime increases from 28 s to 82 s as the initial residual strain increase from 0.28 to 0.58. Two underlying time and microstructure dependent recovery mechanisms could be at the origin of the observed phenomenological trends. Among them, the two aforementioned ones could be possible candidates, *i.e.*, viscoelasticity of EVA together with gas pressure and gas flow between connected cells. For the last possible submechanisms, gas-flow through possible (small) holes in cell walls and re-diffusion through cell walls [49] could be involved. Presumably, the related characteristic times of the second one are too large compared to those involved during cycling and recovery, so that its effects could be considered as negligible [23].
- After 3 h, the recovery was negligible whatever the investigated testing condition. Hence, above such a resting time, the recorded residual strain can be considered as irreversible and permanent: it will be named plastic strain afterwards. Firstly, this point proved that the 3D imaging we performed at 16 h must have been carried out (i) in stable imaging conditions that were (ii) representative of the observed steady state plastic deformation. Secondly, it is interesting to notice that such a plastic deformation is an increasing function of the residual strain after cycling which is in

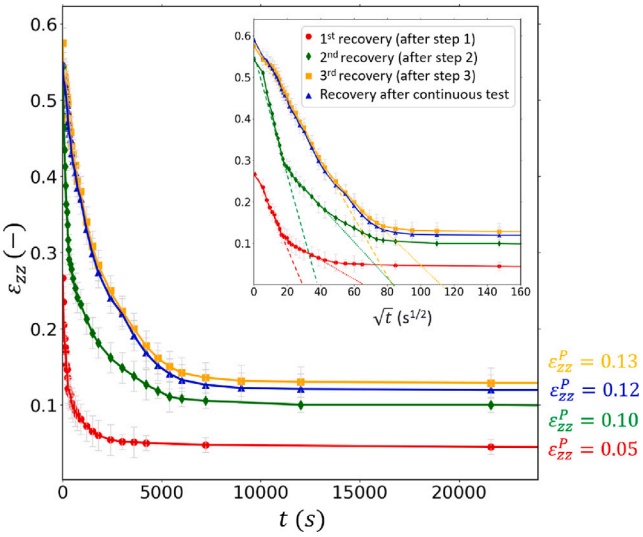

Fig. 7. Main graph: evolution of the recovery strain ε_{zz}^{res} with time t for the various cycling steps used for the interrupted or the continuous cycling procedures. The inset gives a zoom of the early stages of the recovery processes as a function of $\sqrt{t}$.

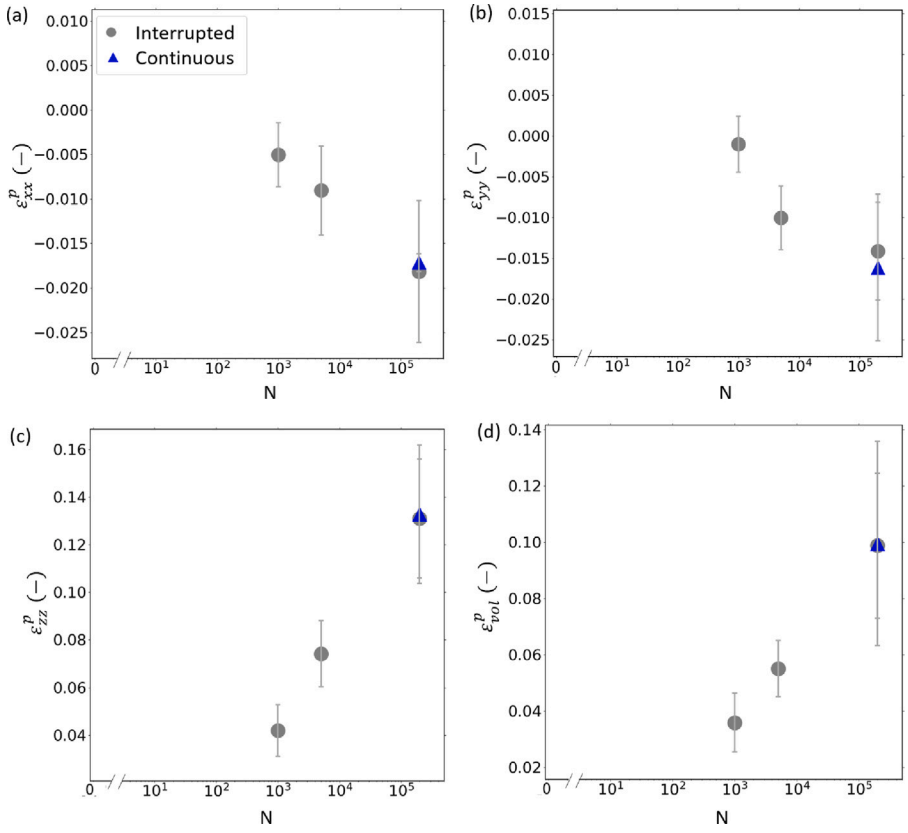

Fig. 8. Evolution of the strain components perpendicular (ε_{xx}^{p} (a), ε_{yy}^{p} (b)) and parallel (ε_{zz}^{p}, (c)) to the compression direction z and of the volume strain ε_{vol}^{p} (d) as functions of the number of cycles N, recorded during the interrupted (•) and the continuous (▲) cycling procedures.

turn an increasing function of the number of cycles N in steady state conditions. As shown in the figure, ε_{zz}^{p} increases from ≈ 0.05 to ≈ 0.13 by increasing the number of cycles. Here again, this figures also shows that such plastic strains do not depend on the studied cycling procedure: practically the same value is reported at the end of the interrupted or the continuous procedures.

- The plastic deformation states observed after recovery are further analyzed thanks to the graphs plotted in Fig. 8 deduced from X-ray microtomography and DVC. Firstly, it is worth noticing that the plastic strain ε_{zz}^{p} obtained at the sample scale (Fig. 7) and from the ROIs (Fig. 8c) are very close. The small differences could be ascribed to some strain heterogeneities in the sample during cycling. Secondly, whatever the considered plastic strain, the graphs of Fig. 8 prove that (i) the magnitude of these plastic strains are increasing functions of the number of cycles, which is a clear fatigue-induced effect, (ii) such increases do not depend on the cycling procedures (see the superimposed blue and gray marks plotted in the graphs), which emphasizes

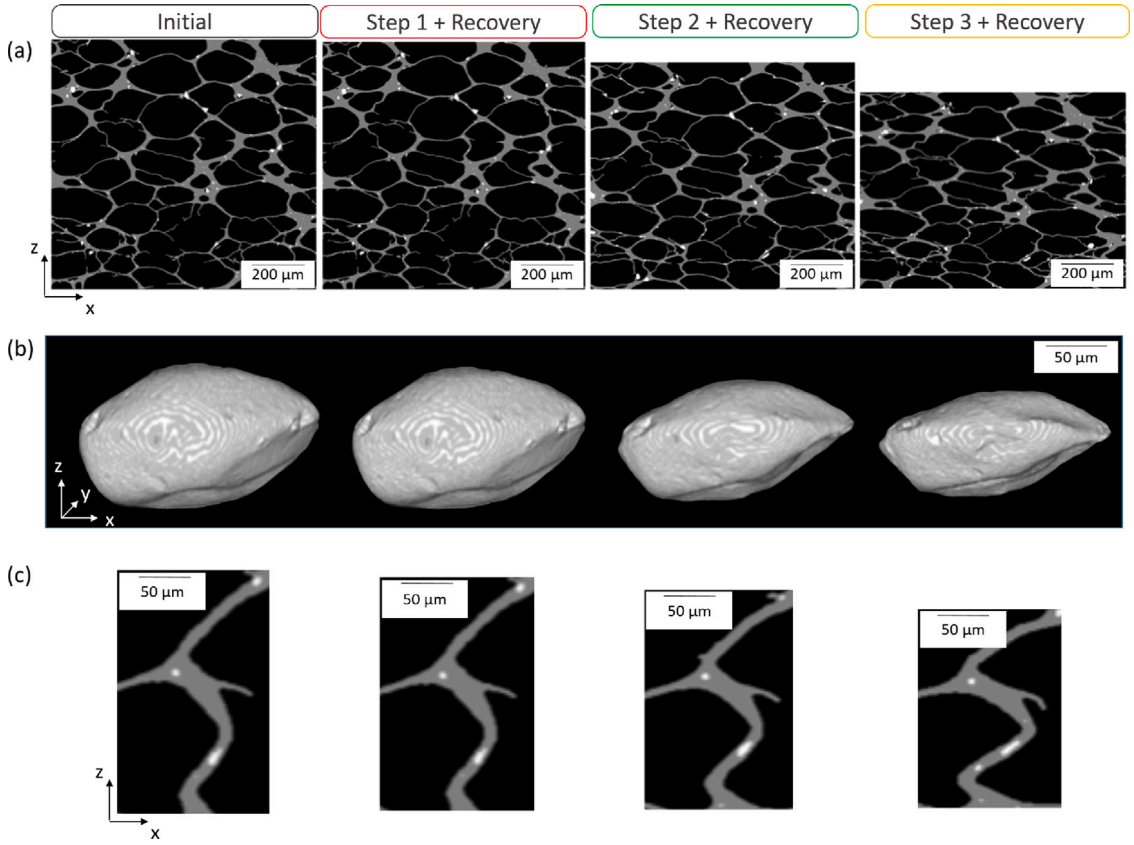

Fig. 9. Structural characterization during *ex situ* interrupted fatigue procedure obtained by X-ray microtomography, (a) at the foam scale, (b) at the cell scale, (c) at the cell-wall scale.

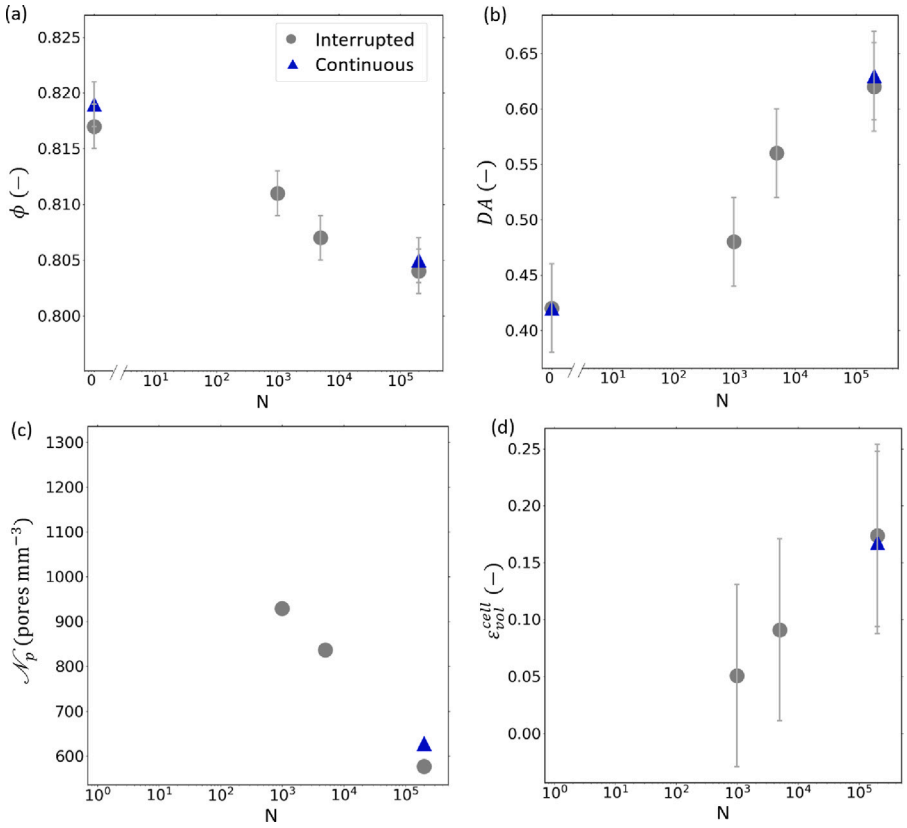

Fig. 10. Structural evolution during the interrupted (◦) and the continuous (▲) cycling procedures as function of the number of compression cycles N: (a) porosity ϕ, (b) average degree of anisotropy of cell DA, (c) apparent volumetric number of pores $\mathcal{N}_p$ (d) cell volume strain ε_{vol}^{cell}.

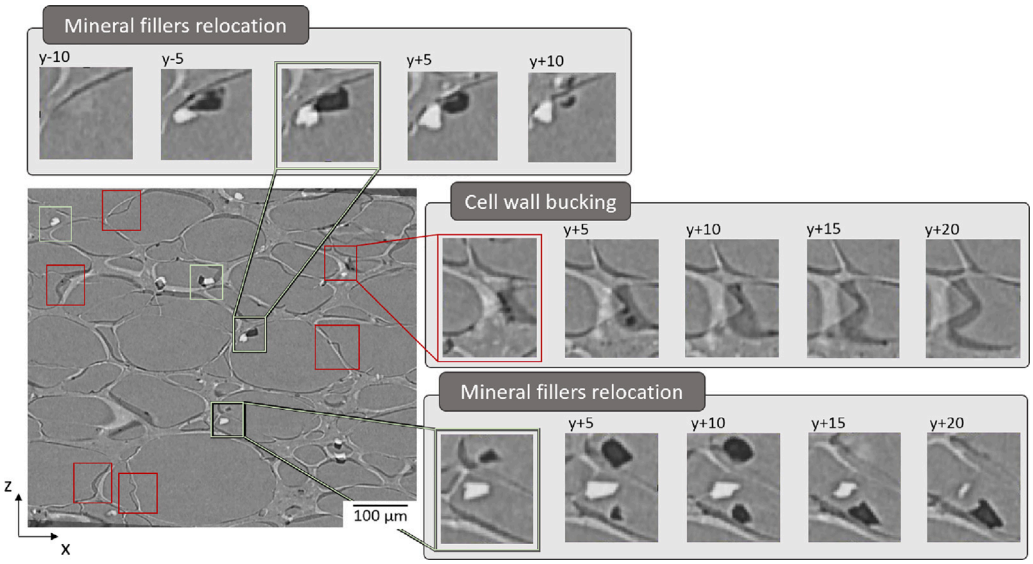

Fig. 11. Slice showing the difference between the initial 3D image and the final registered 3D one. When both images perfectly overlap on one voxel, the resulting value is 0 and appears gray. Values that are highly positives (*i.e.*, the lighter zones) are associated to the initial image, whereas values that are highly negatives (*i.e.*, the darker zones) correspond to the final image. The reported slices highlight the relocation of the mineral charges initially put onto the cell wall and the cell wall bending induced during cycling.

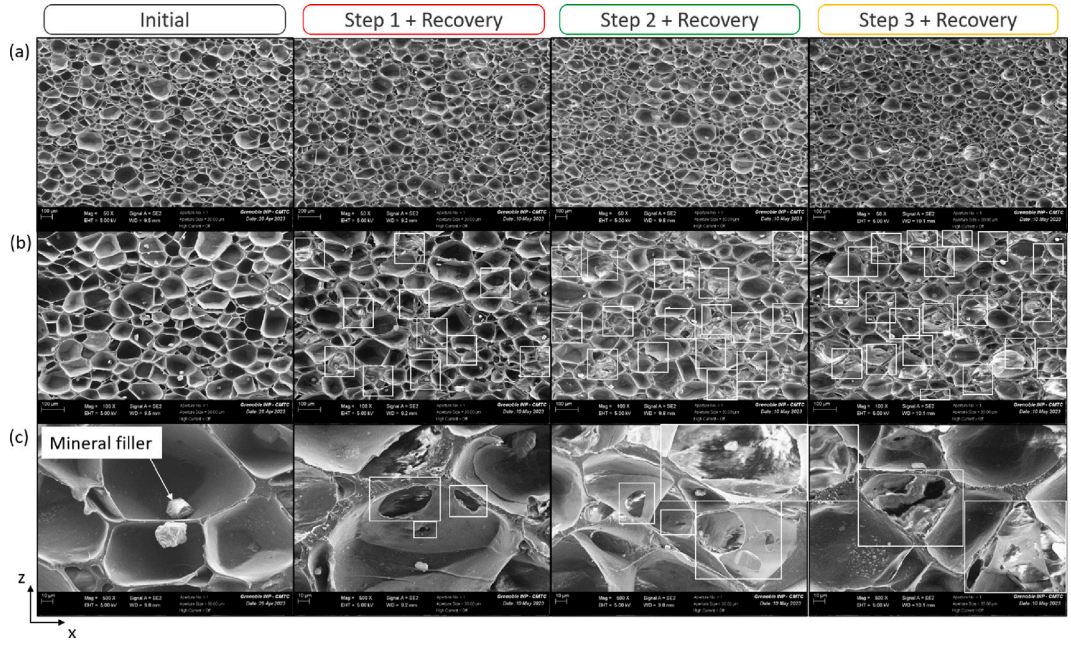

Fig. 12. Structural characterization during *ex situ* interrupted fatigue procedure obtained by SEM, (a) at the sample scale, (b) at the cell scale, (c) at the wall scale. White frames point out the teared cell walls.

here again the foam capability to exhibit erasable memory of subevents (*i.e.*, transient regimes in the interrupted procedure) compared to the main strain path (*i.e.*, the continuous procedure). Thirdly, it must be pointed out that cycling the foam samples induced a pronounced volume variation which is presumably induced by compaction mechanisms at the cell scale (see next subsection): as shown in the graph of Fig. 8d, the plastic volume strain ε^p_{vol} increases up to 0.1 while increasing the number of cycles N. Lastly, it is interesting to notice that the plastic strains orthogonal to the compression axis z, *i.e.*, ε^p_{xx} and ε^p_{yy}, are (i) practically identical, which may be a direct consequence of the initial foam cell structure that exhibits transverse isotropy (see previous subsection), (ii) negative-valued with magnitudes much smaller than the one of ε^p_{zz}. The last point suggests that the cycling-induced foam compaction mechanisms occurred without auxetic/reentrant deformation micro-mechanisms that are prone to occur in other highly deformable cellular systems [31,40].

3.3. Fatigue-induced microstructures

Fig. 4 gives registered slices of the initial and last states of the foam samples deformed according to the interrupted or continuous cycling procedures. Details about what occurred at the end of each sequence of the interrupted procedure are reported in the registered slices of Fig. 9, the corresponding evolving structure descriptors are plotted in the graphs of Fig. 10. Lastly, a closer look at the deformation micro-mechanisms at the cell scale is displayed in the registered micrographs of Fig. 11.

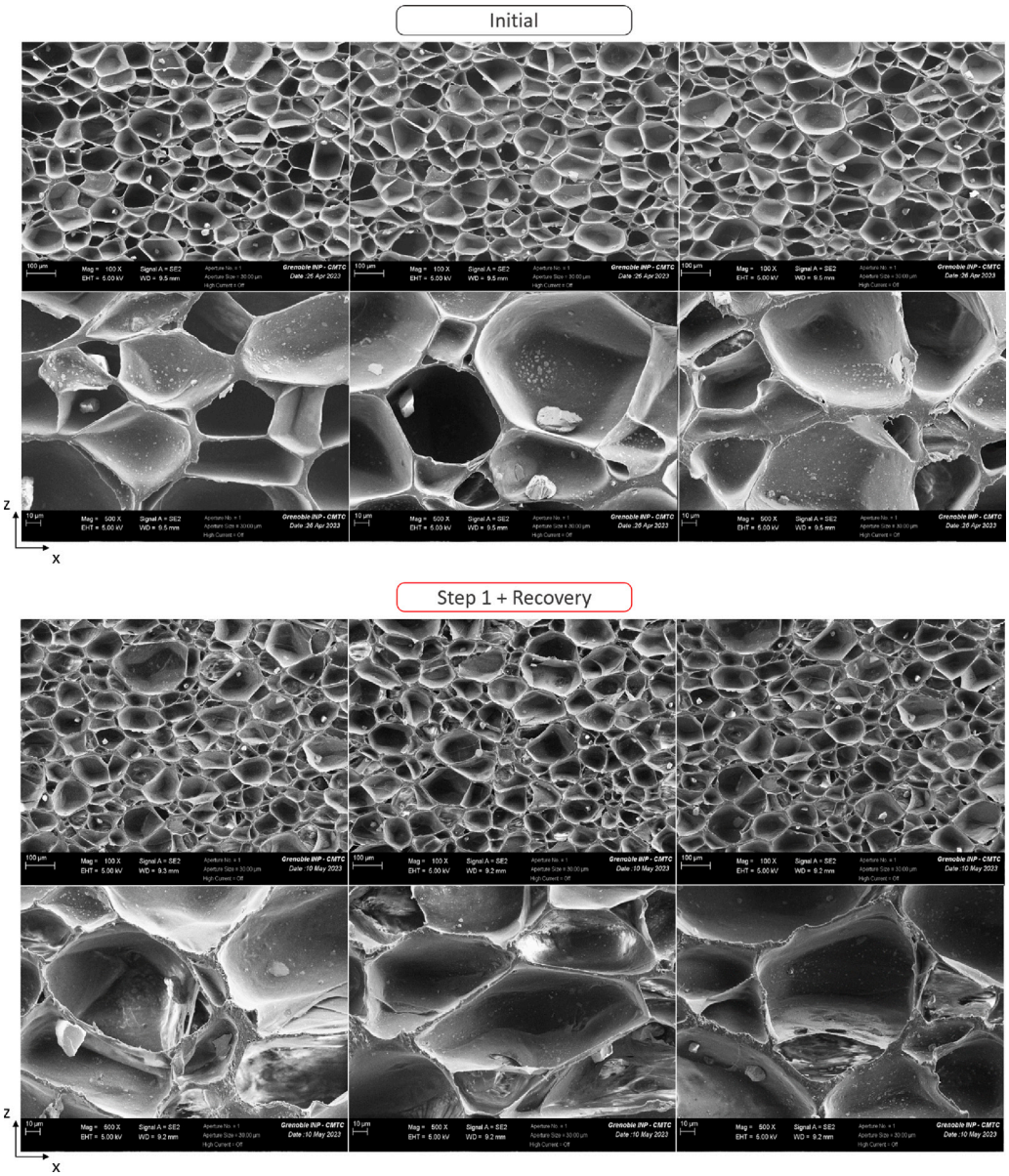

Fig. 13. Additional structural characterization during ex situ interrupted fatigue procedure obtained by SEM at the cell scale and at the wall scale for the initial microstructure and for the microstructure after the first fatigue step and recovery.

Several comments can be conjured up from these figures:

- The micrographs shown in Fig. 4 clearly reveal the structural plastic deformation induced during cycling. This is better highlighted in the 3D images acquired during the interrupted cycling procedure, as evident when scrutinizing Fig. 9. These slices suggest an important compaction mainly occurring along the compression direction z (see, *e.g.*, Fig. 9a) which is in-line with the DVC results reported in Fig. 8. This important compaction yields to a noticeable decrease of the porosity ϕ with the number of cycles N, as shown in Fig. 10a. This decrease is closely linked with the important intrinsic volumetric strains ε_{vol}^{cell} the cells are subjected to, see Fig. 10c.
- At the ROI scale, we also proved that the sample compaction did not occur isotropically (see Fig. 8). This trend is directly related to the plastic shape change the cells exhibit after cycling and recovery. Firstly, the slices shown in Figs. 4, 9a and b, prove that the cell flatten perpendicular to the compression axis z, leading to a progressive and marked increase of the cell degree of anisotropy DA from 0.42 to 0.62, as shown in Fig. 10b. Secondly, a close look at Fig. 4c and d, Fig. 9a and more precisely in Fig. 9c as well as Fig. 11, show that the cell shape is mainly induced by the numerous plastic bending/buckling of cell walls. These deformations mainly occur with cell walls the mid-plane of which were more or less aligned along the compression direction. Their irreversible/plastic shapes suggest fatigue-induced creep mechanisms of the EVA. Also, as revealed by the zooms shown in Figs. 9c and 11, the observed bending mechanisms were probably enhanced by local stress concentrations induced by the mineral fillers in cell walls (Fig. 9c) or to the mineral fillers which could move onto the surface of cell walls upon cycling (Fig. 11).
- The spatial resolution used to perform the 3D images was unfortunately not high enough to properly quantify the possible increase of the decohesion of the interfaces between the mineral fillers and the EVA. This could be a possible additional damage mechanisms that would contribute to the fatigue-induced plasticity of the studied foams.

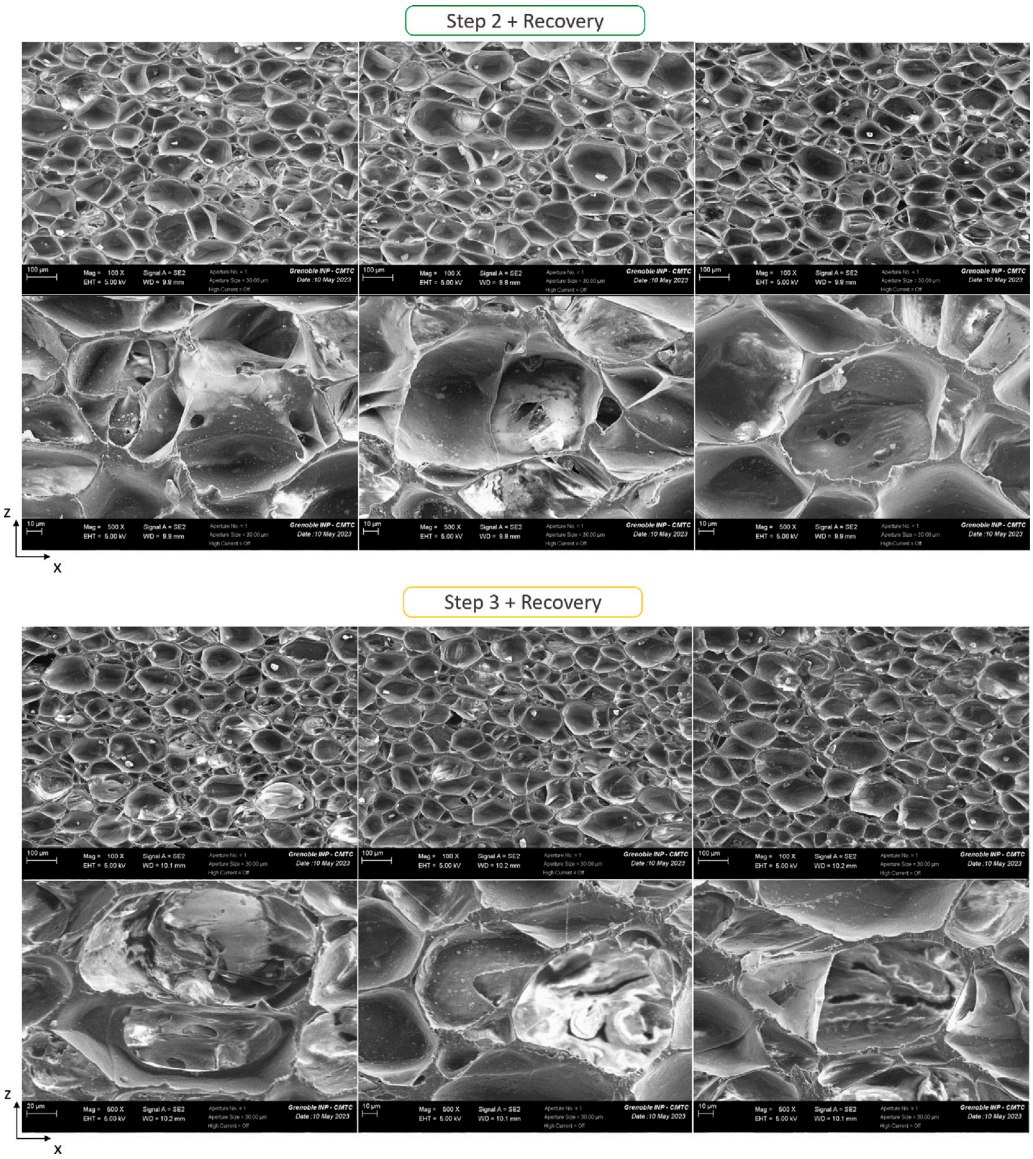

Fig. 14. Additional structural characterization during ex situ interrupted fatigue procedure obtained by SEM at the cell scale and at the wall scale for the microstructure after the second and the third fatigue step and recovery.

- The decreasing evolution of the volumetric number of pores $\mathcal{N}_p$ upon cycling shown in Fig. 10b, *i.e.*, from ≈ 1200 down to ≈ 650 pores mm^{-3} with a faster decrease above $N = 1000$ suggests that cycling the foam samples in compression should be prone to induce more and more connected cells. This trend is confirmed by SEM observation of the damaged structure illustrated in Fig. 12 where the number of teared walls per scanned surface area was counted. The initial microstructure displays closed cells with only 2 teared walls mm^{-2}. The microstructure after the first fatigue sequence and 24 h of recovery exhibits small tears in the very thin cell walls with 13 teared walls per square millimeter. The microstructure after the second fatigue sequence and 24 h of recovery shows more pronounced tearing in the thinner cell walls with 17 teared walls per square millimeter. The microstructure after the last fatigue sequence and 24 h of recovery shows a lot of open cells (*i.e.*, cells with a blurred interior are the result of a partially or completely teared cell wall preventing the SEM from focusing) with only 23 teared walls per square millimeter. Additional observations are given in Appendix. In other words, these results tend to prove that cycling should induce the formation small tears/holes in cell walls, *i.e.*, fatigue-induced damage mechanisms. Their role should be twofold. Firstly, despite the observed plastic compaction which should stiffen the foam mechanics in compression, the mentioned defects should on the contrary soften the foam compression response. Secondly, these tears/holes would also allow an increase of the gas flow between novel connected cells and thus induce additional viscous drag forces. These forces should then (i) increase the damping loss factor η upon cycling, as evidenced in Fig. 6d, (ii) restrain/delay the sample recovery, as evidenced in Fig. 7 too. Thus, these structural evidences reinforce the assumptions we stated at the upper scale in the previous subsection.
- The whole set of graphs plotted in Fig. 10 proves that at the end of cycling, the four evolving structural descriptors, namely ϕ, DA, ϵ_{vol}^{cell} and $\mathcal{N}_p$, exhibit the same respective values, independently of the considered testing procedure: see the last blue and gray marks shown in these graphs. These cell scale results thus strongly reinforce the conclusions we suggested from the stress and strain measurements obtained at the upper scale (see the two last subsections): the studied elastomeric foam exhibit an interesting erasable memory of sub-events such as the "short" transient regimes of the beginning of each sequence of the interrupted

procedure. Also, as a direct consequence of these sample and cell scale observations, the increase of structural damages during the transient cycling regime consecutive to a sufficiently long resting time should probably be minor.

4. Conclusion

The aim of this study was to investigate the fatigue of elastomeric closed-cell foams during finite strain cycling, with a particular focus on the link between the foam mechanical properties during cycling and the structural changes in the foams at the cell scale. For that purpose, we coupled cyclic compression tests at finite strains together with 3D *ex situ* observations of the cell structures using X-ray microtomography and DVC. Two cycling procedures were tested, namely interrupted or continuous ones, with EVA closed-cell foams filled with mineral fillers, widely used for the midsoles of running shoes. The main outcomes of the study are the following:

- Recorded stress–strain curves of the tested EVA foams upon cycling exhibit standard viscoelastoplastic shapes with major elastic effects. Elastic effects are mainly ascribed to the non-linear elasticity of the EVA cell walls, which undergo severe bending/buckling, as well as that of the gas which is entrapped in the cells. Viscous effects observed during cycling are also ascribed to the viscoelasticity of EVA, and to possible viscous drag forces induced by the gas flow through the holes in between the (initially rare) connected cells. Lastly, plastic events may be related to friction at the imperfect interfaces between the mineral fillers (inside or at the surface of cell walls) and the EVA.
- Increasing the number of cycles lead to a progressive and irreversible loss of mechanical properties such as stress levels and absorbed energies. Meanwhile, these features are accompanied with the increase of residual strain and complex evolution of the damping loss factor, with in particular around 1000 cycles, a noticeable shift. In addition, we proved that upon cycling, the plastic strain progressively increases and subsequently causes increasing detrimental (from the application side) compaction of the foams. Three possible fatigue-induced damage mechanisms have been identified at the cell scale to explain these trends: the creep of the EVA cell-walls which yield to their irreversible buckled shapes, the formation of cell-wall tears/holes which exhibit sharper increase above 1000 cycles and may be related to the intermediate increase of the damping loss factor around $N = 1000$ cycles, the progressive decohesion between the mineral fillers and the EVA (we could not quantify properly the last mechanisms because the spatial resolution used to images the samples was too low). Diminishing the size of the mineral charges to restrain cell wall scale stress concentrations which enhance cell wall buckling, optimizing the charge spatial distribution in the EVA as well as the physico-chemical properties of the interfaces would undoubtedly restrain the aforementioned damage mechanisms.
- Interrupting the mechanical cycling lead to a recovery of the foam sample. The recovery is incomplete and its magnitude diminishes mainly because of the increase of damage micromechanisms. In addition, the sample shape recovery is time-dependent, with transient regime exhibiting phenomenological two-stage "Fickian-like diffusion". Possible responsible mechanisms at the cell-scale could be related to the viscoelasticity of the EVA and to the viscous transport of gas between connected cells, respectively.
- Recycling the foams after recovery leads to a rapid ($\approx$ 1000 cycles), sharp and transient decrease of the foam mechanical properties down to the values the sample exhibited before the cycling interruption. By pursuing the cycling above this state, the evolution of the foam mechanical properties recover the trends recorded during continuous cycling, as if the interruption had no effect on the overall fatigue of the foams. We have proved that such an erasable memory is also valid at the cell scale, since the structural properties of the samples does not depend on the investigated cycling procedure, *i.e.*, interrupted or continuous. In other words, cell scale fatigue-induced damage mechanisms should be limited during transient cycling regimes conducted after interruption and complete recovery.

CRediT authorship contribution statement

C. Aimar: Methodology, Investigation, Writing – original draft. **L. Orgéas:** Conceptualization, Methodology, Writing – review & editing, Supervision, Funding Acquisition. **S. Rolland du Roscoat:** Conceptualization, Methodology, Writing – review & editing. **L. Bailly:** Conceptualization, Writing – review & editing. **D. Ferré Sentis:** Conceptualization, Methodology, Writing – review & editing, Funding Acquisition.

Declaration of competing interest

The authors declare the following financial interests/personal relationships which may be considered as potential competing interests: AIMAR reports financial support was provided by ANRT. FERRE SENTIS reports a relationship with Decathlon SportsLab Research and Development that includes: employment.

Data availability

Data will be made available on request.

Acknowledgments

The authors would like to thank Olga Stamati for her help in the use of the freeware *SPAM* and Frédéric Charlot from CMTC for his expertise in the use of the SEM. C. Aimar gratefully acknowledges Decathlon and ANRT, France (2019/1038) for her research grant and financial support. 3SR Lab is part of LabEx Tec 21 (ANR-11-LABX-0030) and of Institut Carnot PolyNat, France (ANR16-CARN-0025).

Appendix. Additional SEM observations

Additional SEM observations of the initial, and the aged structures of samples during the interrupted procedure after the 3 fatigue sequences are presented in Figs. 13 and 14. The number of teared walls per square millimeter has been evaluated as the number of faces damaged on a total scanned surface of 3 mm^3.

References

[1] F.M. de Souza, J. Choi, T. Ingsel, R.K. Gupta, Chapter 6 - high-performance polyurethanes foams for automobile industry, in: Nanotechnology in the Automotive Industry. Micro and Nano Technologies, Elsevier, 2022, http://dx.doi.org/10.1016/B978-0-323-90524-4.00006-2.

[2] T.D. Lickly, K.M. Lehr, G.C. Welsh, Migration of styrene from polystyrene foam food-contact articles, Food Chem. Toxicol. 33 (6) (1995) 475–481, http://dx.doi.org/10.1016/0278-6915(95)00009-Q.

[3] M. Tomin, Á. Kmetty, Polymer foams as advanced energy absorbing materials for sports applications: A review, J. Appl. Polym. Sci. 139 (2021) http://dx.doi.org/10.1002/app.51714.

[4] C. Bathias, P. Houel, Y.N. Berete, K. Legorju, Damage characterization of elastomeric composites using X-ray attenuation, in: Progress in Durability Analysis of Composite Systems, Virginia, USA, ISBN: 90-5410-960-2, 1997, pp. 103–109.

[5] J.B. Le Cam, B. Huneau, E. Verron, Description of fatigue damage in carbon black filled natural rubber, Fatigue Fract. Eng. Mater. Struct. 31 (12) (2008) 1031–1038, http://dx.doi.org/10.1111/j.1460-2695.2008.01293.x.

[6] S. Mzabi, D. Berghezan, S. Roux, F. Hild, C. Creton, A critical local energy release rate criterion for fatigue fracture of elastomers, J. Polym. Sci. B 49 (21) (2011) 1518–1524, http://dx.doi.org/10.1002/polb.22338.

[7] C. Neuhaus, A. Lion, M. Johlitz, P. Heuler, M. Barkhoff, F. Duisen, Fatigue behaviour of an elastomer under consideration of ageing effects, Int. J. Fatigue 104 (2017) 72–80, http://dx.doi.org/10.1016/j.ijfatigue.2017.07.010.

[8] O. Gehrmann, M. El Yaagoubi, H. El Maanaoui, J. Meier, Lifetime prediction of simple shear loaded filled elastomers based on the probability distribution of particles, Polym. Test. 75 (2019) 229–236, http://dx.doi.org/10.1016/j.polymertesting.2019.02.025.

[9] C. Li, H. Yang, Z. Suo, J. Tang, Fatigue-resistant elastomers, J. Mech. Phys. Solids 134 (2020) http://dx.doi.org/10.1016/j.jmps.2019.103751.

[10] S. Hager, T. Craig, Fatigue testing of high performance flexible polyurethane foam, J. Cell. Plast. 28 (3) (1992) http://dx.doi.org/10.1177/0021955X9202800305.

[11] A. Bezazi, F. Scarpa, Mechanical behaviour of conventional and negative Poisson's ratio thermoplastic polyurethane foams under compressive cyclic loading, Int. J. Fatigue 29 (5) (2007) 922–930, http://dx.doi.org/10.1016/j.ijfatigue.2006.07.015.

[12] K. Bouchahdane, N. Ouelaa, A. Belaadi, Static and fatigue compression behaviour of conventional and auxetic open-cell foam, Mech. Adv. Mater. Struct. 29 (27) (2022) 6154–6167, http://dx.doi.org/10.1080/15376494.2021.1972496.

[13] L. Malisoux, N. Delattre, A. Urhausen, D. Theisen, Shoe cushioning, body mass and running biomechanics as risk factors for running injury: A study protocol for a randomised controlled trial, Sports Exerc. Med. (2019) http://dx.doi.org/10.1136/bmjopen-2017-017379.

[14] I.J. Gibson, M.F. Ashby, The mechanics of three-dimensional cellular materials, Proc. R. Soc. Lond. Ser. A Math. Phys. Eng. Sci. 382 (1782) (1982) 43–59, http://dx.doi.org/10.1098/rspa.1982.0088.

[15] T. Allen, M. Pagan, R. Martin, O. Duncan, Effect of rest periods on mechanical ageing of running shoes, Proceedings 49 (1) (2020) 138, http://dx.doi.org/10.3390/proceedings2020049138.

[16] R. Verdejo, N.J. Mills, Performance of EVA foam in running shoes, in: The Engineering of Sport, Vol. 4, Blackwell Science, 2002, pp. 580–588.

[17] H. Kinoshita, B.T. Bates, The effect of environmental temperature on the properties of running shoes, J. Appl. Biomech. 12 (2) (1996) 258–268, http://dx.doi.org/10.1123/jab.12.2.258.

[18] R. Verdejo, N.J. Mills, Heel–shoe interactions and the durability of EVA foam running-shoe midsoles, J. Biomech. 37 (9) (2004) 1379–1386, http://dx.doi.org/10.1016/j.jbiomech.2003.12.022.

[19] N. Lippa, E. Hall, S. Piland, T. Gould, J. Rawlins, Mechanical ageing protocol selection affects macroscopic performance and molecular level properties of ethylene vinyl acetate (EVA) running shoe midsole foam, Procedia Eng. 72 (2014) 285–291, http://dx.doi.org/10.1016/j.proeng.2014.06.082.

[20] R.M. Silva, J.L. Rodrigues, V.V. Pinto, M.J. Ferreira, R. Russo, C.M. Pereira, Evaluation of shock absorption properties of rubber materials regarding footwear applications, Polym. Test. 28 (6) (2009) 642–647, http://dx.doi.org/10.1016/j.polymertesting.2009.05.007.

[21] L. Wang, Y. Hong, J. Li, Durability of running shoes with ethylene vinyl acetate or polyurethane midsoles, J. Sports Sci. 30 (2012) http://dx.doi.org/10.1080/02640414.2012.723819.

[22] Y. Shimazaki, S. Nozu, T. Inoue, Shock-absorption properties of functionally graded EVA laminates for footwear design, Polym. Test. 54 (2016) 98–103, http://dx.doi.org/10.1016/j.polymertesting.2016.04.024.

[23] R. Verdejo, N.J. Mills, Simulating the effects of long distance running on shoe midsole foam, Polym. Test. 23 (5) (2004) 567–574, http://dx.doi.org/10.1016/j.polymertesting.2003.11.005.

[24] N. Lippa, D. Krzeminski, S. Piland, J. Rawlins, T. Gould, Biofidelic mechanical ageing of ethylene vinyl acetate running footwear midsole foam, Proc. Inst. Mech. Eng. P 231 (2016) http://dx.doi.org/10.1177/175433711-6678153.

[25] A. Rizvi, R. Chu, C. Park, Scalable fabrication of thermally insulating mechanically resilient hierarchically porous polymer foams, ACS Appl. Mater. Interfaces 10 (2018) http://dx.doi.org/10.1021/acsami.8b11375.

[26] B.M. Nigg (Ed.), Biomechanics of running shoes, in: Human Kinetics, ISBN: 0-87322-002-1, 1986.

[27] S. Pardo-Alonso, E. Solórzano, L. Brabant, P. Vanderniepen, M. Dierick, L. Van Hoorebeke, et al., 3D analysis of the progressive modification of the cellular architecture in polyureth ane nanocomposite foams via X-ray microtomography, Eur. Polym. J. 49 (5) (2013) 999–1006, http://dx.doi.org/10.1016/j.eurpolymj.2013.01.005.

[28] A. Rack, A. Haibel, B. A, M. B, J. Banhart, Characterization of metal foams with synchrotron tomography and 3D image analysis, in: Proc. 16th World Conference of Nondestructive Testing, 2004.

[29] C. Appoloni, C. Fernandes, M. Innocentini, Á. Macedo, Ceramic foams porous microstructure characterization by X-ray microtomography, Mater. Res. 7 (2004) 557–564, http://dx.doi.org/10.1590/S1516-14392004000400008.

[30] L. Orgéas, S. Gupta, F. Martoïa, P.J.J. Dumont, Ice-templating hydrogels with high concentrations of cellulose nanofibers to produce architected cellular materials for structural applications, Mater. Des. 223 (2022) 111201, http://dx.doi.org/10.1016/j.matdes.2022.111201.

[31] R. Lakes, Foam structures with a negative Poisson 's ratio, Science 235 (4792) (1987) 1038–1040.

[32] S. Dezecot, V. Maurel, J.Y. Buffiere, F. Szmytka, A. Koster, 3D characterization and modeling of low cycle fatigue damage mechanisms at high temperature in a cast aluminum alloy, Acta Mater. 123 (2017) 24–34, http://dx.doi.org/10.1016/j.actamat.2016.10.028.

[33] S. Pardo-Alonso, E. Solórzano, J. Vicente, L. Brabant, M.L. Dierick, I. Manke, et al., Micro-CT-based analysis of the solid phase in foams : Cell wall corrugation and other microscopic features, Microsc. Microanal. 21 (5) (2015) 1361–1371, http://dx.doi.org/10.1017/S1431927615014890.

[34] B.M. Patterson, N.L. Cordes, K. Henderson, J.J. Williams, T. Stannard, S.S. Singh, et al., In situ X-ray synchrotron tomographic imaging during the compression of hyper-elastic polymeric materials, J. Mater. Sci. 51 (1) (2016) 171–187, http://dx.doi.org/10.1007/s10853-015-9355-8.

[35] A.S.S. Singaravelu, J.J. Williams, J. Ruppert, M. Henderson, C. Holmes, N. Chawla, In situ X-ray microtomography of the compression behaviour of eTPU bead foams with a unique graded structure, J. Mater. Sci. 56 (8) (2020) 5082–5099, http://dx.doi.org/10.1007/s10853-020-05621-3.

[36] S. Pérez-Tamarit, E. Solórzano, A. Hilger, I. Manke, M.A. Rodríguez-Pérez, Multi-scale tomographic analysis of polymeric foams: A detailed study of the cellular structure, Eur. Polym. J. 109 (2018) 169–178, http://dx.doi.org/10.1016/j.eurpolymj.2018.09.047.

[37] C. Jailin, A.A. Bouterf, M. Poncelet, S. Roux, In situ microCT-scan mechanical tests: Fast 4D mechanical identification, Exp. Mech. (2017) http://dx.doi.org/10.1007/s11340-017-0305-z.

[38] T. Leißner, A. Diener, E. Löwer, R. Ditscherlein, K. Krüger, A. Kwade, et al., 3D ex-situ and in-situ X-ray CT process studies in particle technology – a perspective, Adv. Powder Technol. 31 (1) (2020) 78–86, http://dx.doi.org/10.1016/j.apt.2019.09.038.

[39] J.J.A. D'haen, M. May, C. Boegle, S. Hiermaier, Damage evolution analysis on compression-loaded multidirectional carbon fiber laminates using ex-situ CT scans, J. Compos. Sci. 6 (2) (2022) 63, http://dx.doi.org/10.3390/jcs6020063.

[40] F. Martoïa, T. Cochereau, P.J.J. Dumont, L. Orgéas, M. Terrien, M.N. Belgacem, Cellulose nanofibril foams: Links between ice-templating conditions, microstructures and mechanical properties, Mater. Des. 104 (2016) 376–391, http://dx.doi.org/10.1016/j.matdes.2016.04.088.

[41] C. Aimar, L. Orgéas, S. Rolland du Roscoat, L. Bailly, D. Ferré Sentis, Compression fatigue of elastomeric foams used in midsoles of running shoes, Footwear Sci. (2023) Submitted version. URL: https://www.dropbox.com/scl/fo/d6sso67vywc8h2ftau0dj/h?dl=0&rlkey=5wf9asg7j1urtkwikcdfjgmwr.

[42] T.E. Clarke, E.C. Frederick, L.B. Cooper, Effects of shoe cushioning upon ground reaction forces in running, Int. J. Sports Med. 4 (4) (1983) 247–251, http://dx.doi.org/10.1055/s-2008-1026043.

[43] B. Gadot, Entangled single-wire NiTi material: A porous metal with tunable superelastic and shape memory properties, Acta Mater. 13 (2015) http://dx.doi.org/10.1016/j.actamat.2015.06.018.

[44] J. Schindelin, I. Arganda-Carreras, E. Frise, V. Kaynig, M. Longair, T. Pietzsch, et al., Fiji: An open-source platform for biological-image analysis, Nature Methods 9 (7) (2012) 676–682, http://dx.doi.org/10.1038/nmeth.2019.

[45] O. Stamati, E. Andò, E. Roubin, R. Cailletaud, M. Wiebicke, G. Pinzon, et al., 'Spam': Software for practical analysis of materials, J. Open Source Softw. 5 (51) (2020) 2286, http://dx.doi.org/10.21105/joss.02286.

[46] I. Arganda-Carreras, V. Kaynig, C. Rueden, K.W. Eliceiri, J. Schindelin, A. Cardona, et al., Trainable weka segmentation: A machine learning tool for microscopy pixel classification, Bioinformatics 33 (15) (2017) 2424–2426, http://dx.doi.org/10.1093/bioinformatics/btx180.

[47] B. Schmid, J. Schindelin, A. Cardona, M. Longair, M. Heisenberg, A high-level 3D visualization API for java and imagej, BMC Bioinformatics 11 (1) (2010) 274, http://dx.doi.org/10.1186/1471-2105-11-274.

[48] V. Boulos, L. Salvo, V. Fristot, P. Lhuissier, D. Houzet, Investigating performance variations of an optimized GPU-ported granulometry algorithm, in: DASIP 2012 - Conference on Design and Architectures for Signal and Image Processing, Karlsruhe, Germany, 2012, pp. 1–6.

[49] M.Á. Rodríguez-Pérez, J.L. Ruiz-Herrero, E. Solórzano, J.A. de Saja, Gas diffusion in polyolefin foams during creep tests. Effect on impact behaviour and recovery after creep, Cell. Polym. 25 (2006) 221–236, http://dx.doi.org/10.1177/026248930602500402.